



A hypoxia responsive nanoassembly for tumor specific oxygenation and enhanced sonodynamic therapy

Kuikun Yang^{a,1}, Ludan Yue^{a,1}, Guocan Yu^b, Lang Rao^b, Rui Tian^b, Jianwen Wei^a,
Zhiqing Yang^{a,1}, Chen Sun^a, Xiangjun Zhang^a, Mengze Xu^c, Zhen Yuan^c, Xiaoyuan Chen^{d,e,f,*},
Ruibing Wang^{a,**}

^a State Key Laboratory of Quality Research in Chinese Medicine, Institute of Chinese Medical Science, University of Macau, Avenida da Universidade, Taipa, Macau, China

^b National Institute of Biomedical Imaging and Bioengineering, National Institutes of Health, Bethesda, MD, 20892, USA

^c Cancer Centre, Faculty of Health Sciences, and Centre for Cognitive and Brain Sciences, University of Macau, Avenida da Universidade, Taipa, Macau, China

^d Departments of Diagnostic Radiology, Chemical and Biomolecular Engineering, and Biomedical Engineering, National University of Singapore, Singapore

^e Clinical Imaging Research Centre, Centre for Translational Medicine, Yong Loo Lin School of Medicine, National University of Singapore, Singapore

^f Nanomedicine Translational Research Program, NUS Center for Nanomedicine, Yong Loo Lin School of Medicine, National University of Singapore, Singapore

ARTICLE INFO

Keywords:

Self-assembly
Hypoxia-responsive
Tumor oxygenation
Sonodynamic therapy

ABSTRACT

The hypoxic tumor microenvironment (TME) and non-specific distribution of sonosensitizers are two major obstacles that limit practical applications of sonodynamic therapy (SDT) in combating tumors. Here we report a hypoxia-responsive nanovesicle (hMVs) as delivery vehicles of a sonosensitizer to enhance the efficacy of SDT via specific payload release and local oxygenation in the tumor. The nanovesicles are composed of densely packed manganese ferrite nanoparticles (MFNs) embedded in hypoxia-responsive amphiphilic polymer membranes. With δ -aminolevulinic acid (ALA) loaded in the hollow cavities, the hMVs could rapidly dissociate into discrete nanoparticles in the hypoxic TME to release the payload and induce the generation of reactive oxygen species (ROS) under ultrasound (US) radiation. Meanwhile, the released MFNs could catalytically generate O_2 to overcome the hypoxic TME and thus enhance the efficacy of SDT. After treatment, the dissociated MFNs could be readily excreted from the body via renal clearance to reduce long term toxicity. *In vitro* and *in vivo* experiments displayed effective tumor inhibition via hMVs-mediated SDT, indicating the great potential of this unique nanoplatform in effective SDT by generating sufficient ROS in deep-seated hypoxic tumors that are not readily accessible by conventional photodynamic therapy.

1. Introduction

Sonodynamic therapy (SDT) has emerged as a noninvasive therapeutic strategy for a variety of cancers by activating sonosensitizers to generate reactive oxygen species (ROS) under ultrasound (US) radiation to induce cancer cell apoptosis with minimal damage to healthy tissues [1–4]. In contrast to traditional light-based photodynamic therapy (PDT), SDT exhibits deeper penetration into tumor tissues, allowing the treatment of large or deep-seated tumors [5–7]. However, the hypoxic

tumor microenvironment (TME) significantly restricts the antitumor efficacy of SDT due to a lack of O_2 that is essential for ROS generation in deep tumor tissues. In addition, the rapid O_2 consumption during the SDT process would deteriorate tumor hypoxia, further reducing the therapeutic efficacy of SDT and aggravating tumor growth and metastasis [8,9].

Various oxygen-delivery strategies have been developed to improve SDT efficacy by modulating the hypoxic TME. For instance, nano-materials loaded with both O_2 generators (such as catalase, MnO_2 and Pt

* Corresponding author. Departments of Diagnostic Radiology, Chemical and Biomolecular Engineering, and Biomedical Engineering, National University of Singapore, Singapore, 117545, Singapore.

** Corresponding author. State Key Laboratory of Quality Research in Chinese Medicine, Institute of Chinese Medical Science, University of Macau, Avenida da Universidade, Taipa, Macau, China.

E-mail addresses: chen.shawn@nus.edu.sg (X. Chen), rwang@um.edu.mo (R. Wang).

¹ K. Y., L.Y. and Z. Y. contributed equally to this work.

<https://doi.org/10.1016/j.biomaterials.2021.120822>

Received 9 December 2020; Received in revised form 5 April 2021; Accepted 9 April 2021

Available online 3 May 2021

0142-9612/© 2021 Elsevier Ltd. All rights reserved.

nanoparticles) and sonosensitizers have been reported to efficiently relieve tumor hypoxia and enhance the SDT efficacy [10–12]. However, these oxygen-delivery strategies often suffer from poor biocompatibility, instability and transitory O₂ generation. More significantly, the non-specific release of O₂ generators and sonosensitizers *in vivo* may lead to compromised therapeutic efficacy and severe side effects under US stimulation [13–15]. Therefore, it is essential to selectively deliver O₂ and sonosensitizers to tumor tissues for effective and safe SDT.

Here we develop a hypoxia-responsive nanovesicle (hMVs) to selectively deliver sonosensitizers and generate O₂ in hypoxic TME for enhanced, tumor-specific SDT (Fig. 1). The vesicles are assembled from poly (ethylene oxide)-*b*-poly(6-(2-nitroimidazol-1-yl)hexyl methacrylate) (PEO-*b*-PNIHM)-tethered manganese ferrite nanoparticles (MFNs), and loaded with δ -aminolevulinic acid (ALA), one U.S. Food and Drug Administration approved agent, in their hollow cavities [16]. After intravenous (*i.v.*) administration, the ALA-loaded MFN vesicles (ALA-hMVs) could remain stable under normoxic conditions to prevent non-specific leakage of ALA, and passively accumulate in tumors owing to the enhanced permeability and retention (EPR) effect. The hydrophobic 2-nitroimidazoles on the amphiphilic block copolymers (BCPs) could be transferred into hydrophilic 2-aminoimidazoles in the hypoxic TME after a series of reactions [17–19]. As a result, the ALA-hMVs dissociate specifically in the tumor to release ALA, which would be transformed into protoporphyrin IX (PpIX) to induce ROS generation under US stimulation [20,21]. Meanwhile, the dissociated ALA-hMVs could also release MFNs as efficient catalysts to generate O₂ from overexpressed H₂O₂ in the TME to promote the SDT efficacy [22,23]. Owing to the ultrasmall sizes after *in vivo* dissociation and decomposition, the released MFNs undergo rapid renal clearance to ensure minimized long term toxicity. Consequently, the local generation of PpIX and O₂ in tumor tissues could significantly enhance the therapeutic efficacy and reduce potential side effects of SDT, providing a promising strategy for SDT-based tumor elimination.

2. Results

Synthesis and characterization of ALA-hMVs. Oleic acid-capped MFNs (11.7 ± 0.7 nm in diameter) were prepared by thermal

decomposition as reported previously (Figure S1–S3) [24]. Hypoxia-responsive BCPs of PEO₄₅-*b*-PNIHM₃₆ were synthesized and attached onto MFNs via the thiol-ene click reaction to obtain amphiphilic colloidal nanoparticles (Figure S4–S7) [25,26]. The average graft density of BCPs was estimated to be 0.04 chains/nm [2] according to thermogravimetric analysis (Figure S8) [27]. The hMVs were assembled from amphiphilic BCP-attached MFNs (BCP-MFNs) by a solvent exchange method owing to the hydrophobicity-driven conformational change of BCPs on nanoparticle surface, as was reported previously (Fig. 2A) [28,29]. Scanning and transmission electron microscopy (SEM/TEM) images exhibit well-defined vesicular structures of the nanoassemblies with uniform size distributions, and the hollow interior of hMVs can be clearly observed from these vesicles (Fig. 2B, C, S9 and S10). The hMVs are composed of a monolayer of polymer membrane bearing densely packed MFNs and the vesicular nanoassemblies were verified by the high-angle annular dark-field scanning TEM and EDS element mapping (Fig. 2D–F). The hydrodynamic diameter of the hMVs was estimated to be 129.9 ± 16.3 nm according to the dynamic light scattering (DLS) analysis (Fig. 2G), which is beneficial for passive tumor accumulation via the EPR effect [30,31].

The hMVs remained stable for over 30 days in phosphate-buffered saline (PBS) supplemented with 10% fetal bovine serum (Figure S11). In the presence of nitroreductases and NADH to mimic the hypoxic TME, hMVs dissociated completely within 2 h as evidenced by the TEM and DLS analysis (Fig. 2H, S12). This could be attributed to the reduction of hydrophobic 2-nitroimidazoles to hydrophilic 2-aminoimidazoles under hypoxic conditions (Figure S13). As a result, the amphiphilic building blocks of BCP-MFNs turned into more hydrophilic nanoparticles, leading to the hypoxia-responsive dissociation of hMVs owing to the weakened hydrophobic-hydrophobic interactions. The hypoxia-induced disassembly was accompanied by the release of ALA from ALA-hMVs (Fig. 2I). ALA-hMVs exhibited a rapid release of over 90.5% of ALA within 3 h incubation under hypoxic conditions. In contrast, less than 10% of all loaded ALA was released from ALA-hMVs under normoxic conditions for up to 5 h, indicating the hypoxia-induced dissociation of the nanocarriers is a prerequisite for the release of ALA from the vesicles. Apart from the release of ALA to induce tumor specific SDT, hypoxia-responsive dissociation of the nanoassemblies into individual MFNs

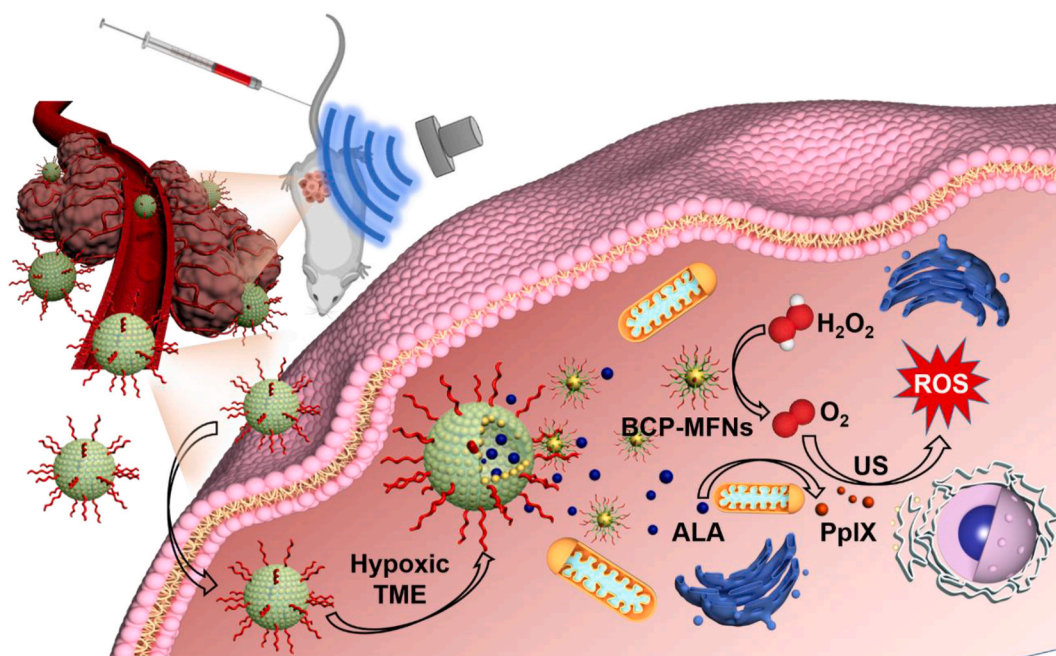


Fig. 1. The design principle of nanoassembly-induced tumor oxygenation and augmented SDT. Schematic illustration of ALA-hMVs for hypoxia-responsive SDT of tumors.

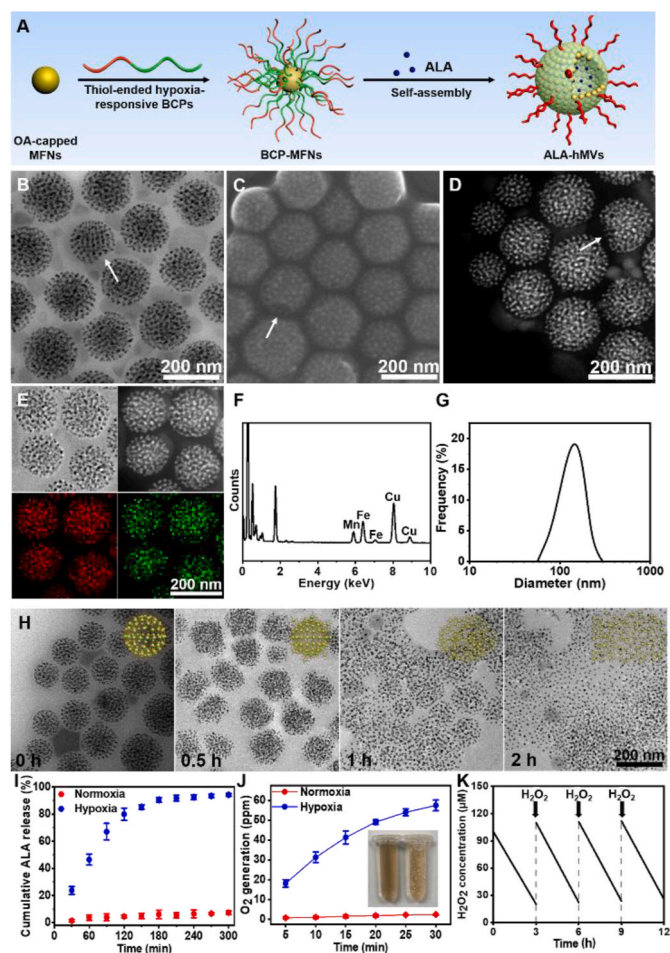


Fig. 2. Synthesis and characterization of ALA-hMVs. (A) Schematic illustration showing the assembly of BCP-tethered MFNs into ALA-hMVs. (B) Representative TEM, (C) SEM and (D) high-angle annular dark-field scanning TEM images of monolayered hMVs self-assembled from BCP-tethered MFNs. (E) EDS element mapping and (F) EDS spectrum of hMVs. (G) The size distribution of hMVs measured by DLS. (H) TEM images of hMVs incubated with nitroreductases and NADH for various durations. (I) *In vitro* release of ALA from ALA-hMVs under normoxic and hypoxic conditions, respectively. (J) Generation of O₂ from normoxia and hypoxia-pretreated hMVs in the presence of 100 μM H₂O₂. Inset: image of H₂O₂ solutions containing normoxia pre-treated hMVs (left) and hypoxia pretreated hMVs (right), respectively. (K) Repeating catalytic activity of dissociated hMVs after repetitive supplement of H₂O₂.

could also initiate selective O₂ generation in tumors. To assess the catalytic activity of intact and dissociated nanoassemblies, hMVs were pretreated under normoxic and hypoxic conditions respectively, followed by the addition of a H₂O₂ solution at an endogenous concentration (100 μM). The hypoxia pretreated hMVs exhibited significant consumption of H₂O₂ and production of O₂ readily after addition into 100 μM H₂O₂ solution (Fig. 2J and S14). In contrast, no significant change in H₂O₂ or O₂ concentrations was observed for hMVs pretreated under normoxic conditions, suggesting that the hypoxia-induced dissociation of hMVs is essential for efficient catalytic generation of O₂ from endogenous H₂O₂. As hMVs remained intact under normoxic conditions, the H₂O₂ solution had limited accessibility to MFNs entrapped in the hydrophobic polymer membrane of the vesicles, resulting in a low catalytic activity of the assemblies. However, hMVs could dissociate into individual hydrophilic nanoparticles under hypoxic conditions, enabling sufficient contact between H₂O₂ and the nanoparticles. As a result, H₂O₂ was decomposed rapidly into O₂ under the catalytic effect of dissociated MFNs, leading to selective oxygenation in the hypoxic TME. In addition, the dissociated hMVs exhibited continuous generation

of O₂ with repetitive supplement of H₂O₂, indicating that the sustainable catalytic activity of the dissociated hMVs may relieve and even reverse the hypoxic TME (Fig. 2K). For comparison, hypoxia-inert BCPs of poly(ethylene oxide)-*b*-polystyrene (PEO-*b*-PS) and non-catalytic iron oxide nanoparticles were fabricated for the construction of non-responsive MVs (nMVs) and non-catalytic ferro-vesicles (hFVs) for the following studies, respectively (Figure S15–S20).

Hypoxia-responsive oxygenation and enhanced SDT *in vitro*. To investigate the catalytic activity of hMVs *in vitro*, the expression of hypoxia-inducible factor 1-α (HIF-1α) protein in B16 tumor cells was measured to evaluate the degree of hypoxia at the cellular level (Fig. 3A) [32,33]. Compared with the low expression of HIF-1α in normoxia-treated B16 cells, strong red fluorescence was found in cells incubated with PBS, nMVs or hFVs in hypoxia, indicating the upregulated expression of intracellular HIF-1α in the hypoxic environment. However, significantly reduced expression of HIF-1α was found in cells incubated with hMVs in hypoxia, suggesting a dramatic alleviation of hypoxia due to the dissociation of hMVs and subsequent MFN-mediated O₂ generation. This hypoxia-responsive disassembly of hMVs was confirmed by TEM observation of hMVs-treated B16 cells under normoxic and hypoxic conditions, respectively (Figure S21). In contrast to the intact nanovesicles in normoxia-treated cells, disassembled vesicles as well as individual MFNs were found in cells under hypoxic incubation.

Apart from the selective generation of O₂, the hypoxia-induced dissociation of ALA-hMVs could also initiate the release and conversion of ALA into PpIX as a sonosensitizer for tumor specific SDT. The cellular uptake of the nanocarriers and intracellular generation of PpIX were evaluated by monitoring the red fluorescence of PpIX in B16 cells (Figure S22 and S23). The cells exhibited a 14.6 and 20.4-fold increase in intracellular fluorescence after incubation with ALA-hMVs for 12 h under hypoxic conditions as compared with those treated with ALA-hMVs in normoxia or with ALA-nMVs in hypoxia respectively, indicating the rapid hypoxia-induced disassembly of ALA-hMVs, release of ALA and subsequent conversion of ALA into PpIX in tumor cells. The intracellular ROS were measured with 2,7-dichlorofluorescein diacetate (DCFH-DA) as the ROS probe (Fig. 3B–D). Upon US radiation, the ALA-hMVs treated cells exhibited apparently stronger green fluorescence under hypoxic conditions than normoxic conditions. In addition, no significant fluorescence was found in cells treated with ALA, hMVs, ALA-nMVs or ALA-hFVs under hypoxic conditions. The enhanced production of ROS in ALA-hMVs treated cells could be ascribed to 1) hypoxia-induced disassembly of the nanocarriers and release of ALA that is subsequently converted into PpIX, and 2) catalytic O₂ generation after dissociation of the vesicles. Notably, no ROS generation was found in cells in the absence of US, indicating that hypoxia-induced release of ALA, selective generation of O₂ as well as US radiation are prerequisites for efficient generation of ROS by ALA-hMVs in tumor cells (Figure S24 and S25). The therapeutic efficacy of ALA-hMVs-augmented SDT was evaluated on B16 cells under normoxic or hypoxic conditions via 3-(4,5-dimethylthiazol-2-yl)-2,5-diphenyltetrazolium bromide (MTT) assays (Fig. 3E and S26) [34]. No significant cytotoxicity was found in all groups without US radiation, indicating the outstanding biocompatibility of the vesicles. ALA-hMVs exhibited a dose-dependent cytotoxicity on B16 cells incubated under hypoxic conditions and US radiation, whereas no obvious toxicity was observed in cells treated with ALA-hMVs under normoxic conditions or with ALA, ALA-nMVs or ALA-hFVs under hypoxic conditions. ALA-hMVs exhibited an IC₅₀ value of 1.04 mM under hypoxic incubation and US radiation, which is 3.2-fold lower than that of free ALA under the same conditions. The enhanced therapeutic efficacy of ALA-hMVs mediated SDT was attributed to the hypoxia-induced release of ALA and selective generation of O₂. Similar results were observed when apoptosis of tumor cells was assessed via the typical Annexin V-FITC and PI double staining protocol (Fig. 3F). ALA-hMVs treated cells exhibited a significantly higher apoptotic rate under hypoxic conditions than any other group,

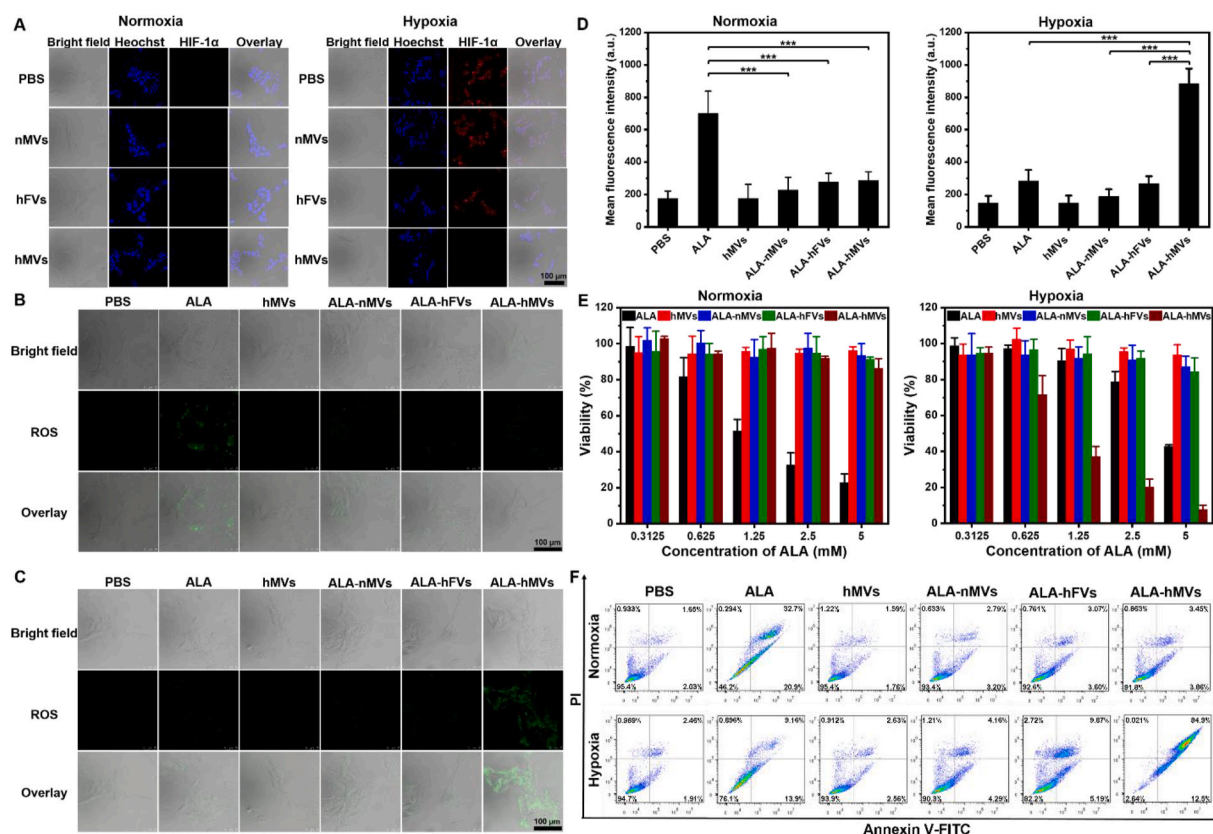


Fig. 3. *In vitro* oxygenation, ROS production and cytotoxicity of ALA-hMVs upon US irradiation under hypoxic conditions. (A) Immunofluorescence staining of HIF-1 α in B16 cells treated with PBS, nMVs, hFVs or hMVs under normoxic and hypoxic conditions, respectively. (B and C) Confocal images and (D) corresponding fluorescence intensity of DCFH-DA-stained, US-irradiated B16 cells after incubation with different ALA-loaded vesicles under (B) normoxic and (C) hypoxic conditions, respectively. (E) Cell viability (via MTT assays) and (F) apoptosis rates (via flow cytometry analysis) of B16 cells under US radiation after different treatments. (***) $p < 0.001$, (**) $p < 0.01$, (*) $p < 0.05$.

indicating the promising potential of ALA-hMVs for hypoxia-responsive SDT.

Biodistribution and hypoxia-responsive tumor oxygenation of ALA-hMVs *in vivo*. ALA-hMVs were labeled with Cy7 on the surface and intravenously injected into B16 tumor bearing mice to investigate the distribution of the vesicles *in vivo* (Figure S27 and S28). The mice were imaged via an *in vivo* imaging system (IVIS) at scheduled time points after *i.v.* injection to trace the distribution of the vesicles (Fig. 4A). The fluorescence signals in tumors exhibited a gradual increase and reached maximum intensity at 24 h post-injection of the nanoassemblies, suggesting the time-dependent accumulation of Cy7-labeled ALA-hMVs in the tumor, likely owing to the EPR effect. After injection of Cy7-labeled ALA-hMVs for 48 h, tumors and major organs of each mouse were harvested for quantitative *ex vivo* imaging (Fig. 4B and C). The tumors exhibited relatively strong fluorescence, suggesting the efficient passive accumulation of the vesicles in the tumor. Notably, strong fluorescence was also found in the livers, lungs and kidneys, likely attributed to the systemic circulation and clearance of small nanoparticles from dissociated hMVs in the hypoxic TME [35–37]. To further investigate the distribution and clearance of the nanoassemblies, the content of Mn in blood, urine, tumors and major organs was closely monitored over time by ICP-MS after *i.v.* administration. The clearance of ALA-hMVs in the blood follow a simple exponential decay curve, with a half-life of ~ 11.7 h (Fig. 4D). The tumor uptake of ALA-hMVs increased from 1.2 ± 0.2 ID% g^{-1} at 2 h post-injection to 13.4 ± 3.8 ID% g^{-1} at 24 h, indicating the efficient accumulation of the nanocarriers in tumors (Fig. 4E). Notably, significantly increased Mn signals were found in kidney at 8 h post-injection ($\sim 5.6 \pm 0.7$ ID% g^{-1}), which reached the maximum of 11.9 ± 3.4 ID% g^{-1} at 36 h, suggesting that the dissociated MFNs might be

readily excreted from the body after treatments via renal clearance. This was confirmed by the increasing Mn content in mice urine after *i.v.* administration of ALA-hMVs (Figure S29). Furthermore, individual MFNs were also observed in mice urine via TEM (Fig. 4F). The renal cleared MFNs were irregular in shape, with significantly reduced overall sizes (3.9 ± 0.6 nm, Figure S30). Therefore the renal clearance of MFNs relied on a two-step decomposition process of ALA-hMVs: 1) the hypoxia-responsive vesicles dissociated readily into individual MFNs after accumulating in the hypoxic tumor site and 2) the released MFNs could be decomposed into ultrasmall nanoparticles *in vivo*, which underwent rapid renal clearance owing to the significantly reduced sizes. Therefore both hypoxia-responsiveness and *in vivo* decomposition of MFNs promoted the rapid renal clearance of the intravenously injected nanoassemblies.

Encouraged by the hypoxia-responsive disassembly, catalytic activity and efficient accumulation of ALA-hMVs in the tumor, we further investigated the oxygenation status of tumors after *i.v.* administration of various vesicles. The tumor vascular saturated O_2 levels (sO_2) were evaluated via photoacoustic (PA) imaging at two excitation wavelengths of 750 nm and 850 nm, respectively (Fig. 5A and B). For the mice injected with PBS, ALA-nMVs or ALA-hFVs, no significant change in sO_2 ($< 2.5\%$) was observed in tumors after the *i.v.* administration, suggesting that the hypoxic TME was retained in these groups of mice. In contrast, an intensely enhanced PA signal at 850 nm was observed in tumors of mice at 6 h post-injection of ALA-hMVs. The tumor vascular sO_2 increased from $1.6 \pm 0.3\%$ (pre-injection) to $13.6 \pm 0.8\%$ at 24 h post-injection of ALA-hMVs, which was 8.3-, 7.5- and 6.9-fold higher than that of the PBS, ALA-nMVs and ALA-hFVs treated mice, indicating efficient oxygenation and hypoxia relief in tumors of the ALA-hMVs treated

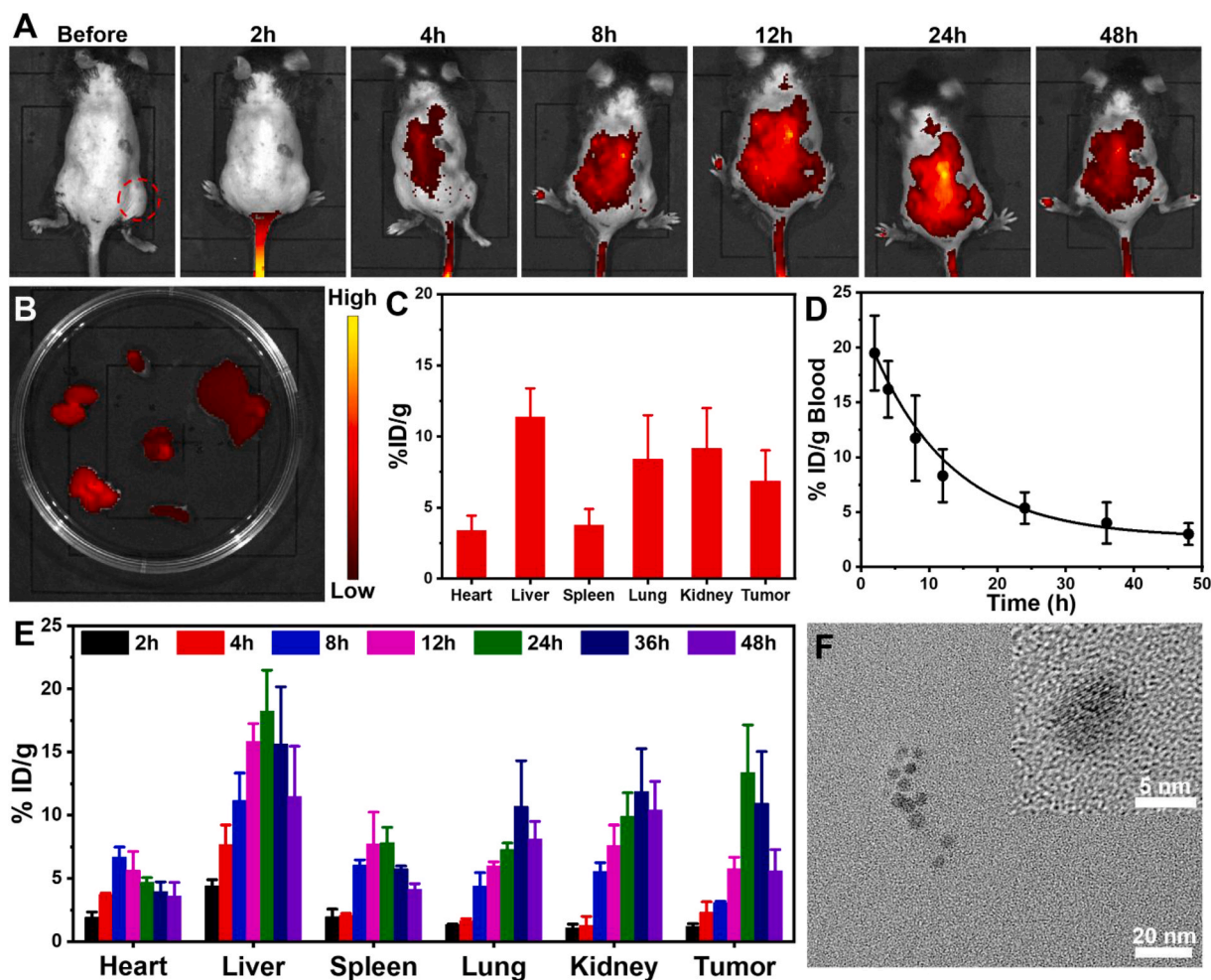


Fig. 4. *In vivo* biodistribution and clearance of ALA-hMVs in B16 tumor-bearing mice. (A) *In vivo* fluorescence imaging of B16 tumor-bearing mice before and after *i.v.* injection of Cy7-labeled ALA-hMVs at different time points. (B) Representative *ex vivo* fluorescence imaging of the tumor and major organs 48 h post-injection of Cy7-labeled ALA-hMVs. (C) Quantification of fluorescence intensity in tumors and major organs 48 h post *i.v.* injection of Cy7-labeled ALA-hMVs ($n = 5$). (D) Blood clearance of ALA-hMVs in B16 tumor bearing mice. (E) Biodistribution of ALA-hMVs in the main organs at different time post-injection ($n = 5$). (F) Representative TEM images of dissociated MFNs in mice urine collected at 24 h post-injection of ALA-hMVs. (** $p < 0.001$, ** $p < 0.01$, * $p < 0.05$).

mice. To further confirm the alleviation of tumor hypoxia by ALA-hMVs, immunofluorescence staining of HIF-1 α in tumor sections was performed at 24 h post-injection of various vesicles (Fig. 5C and D). Compared with PBS, ALA-nMVs and ALA-hFVs treated groups, mice injected with ALA-hMVs showed significantly decreased HIF-1 α signals in the tumor tissues, confirming the efficient tumor oxygenation and hypoxia relief by hypoxia-responsive ALA-hMVs.

***In vivo* inhibition of tumor growth via ALA-hMVs-mediated tumor oxygenation and enhanced SDT.** To further evaluate the therapeutic efficacy of ALA-hMVs-mediated SDT, B16 tumor-bearing C57BL/6 mice were divided into 7 groups ($n = 5$) in a random manner and respectively treated with: (1) PBS, (2) US only, (3) ALA + US, (4) ALA-hMVs, (5) ALA-nMVs + US, (6) ALA-hFVs + US and (7) ALA-hMVs + US (equivalent ALA dose of 50 mg/kg). For the groups of mice involved US treatment, US radiation was applied twice, on Day 0 and Day 3, both at 24 h after *i.v.* injection of ALA or ALA-loaded vesicles. The tumor volume was measured every two days. The mice treated with PBS, US, ALA + US, ALA-hMVs or ALA-nMVs + US all exhibited a rapid increase in the tumor volume (Fig. 6A). Owing to the selective release of ALA in tumors, moderate tumor growth was observed in the mice treated with ALA-hFVs + US, suggesting the limited therapeutic efficiency of SDT on hypoxic tumors without oxygenation. In contrast, the mice treated with ALA-hMVs + US displayed a relatively high tumor inhibition efficiency of 94.6%, suggesting

the significantly improved efficacy of ALA-hMVs-mediated SDT. The lower tumor weight at the end of treatment as well as the much longer survival time of mice treated with ALA-hMVs + US further confirmed the strongest antitumor activity of ALA-hMVs-mediated SDT, when compared with all the other treatment groups (Fig. 6B and C). In addition, the mice treated with ALA-hMVs + US showed the most significant apoptosis and necrosis of cancer cells, according to the hematoxylin and eosin (H&E) staining and the terminal deoxynucleotidyl transferase dUTP nick end labeling (TUNEL) staining of the tumor tissue sections (Fig. 6D and E), suggesting the enhanced SDT efficacy via hypoxia-responsive release of ALA and tumor-specific generation of O₂. Notably, no significant changes in the body weight were observed for the mice of all groups during the treatment, implying the minimal systemic toxicity of the ALA-loaded vesicles (Figure S31). Meanwhile, no obvious damage was observed in the major organs of mice in each group, further proving the excellent biosafety of the nanocarriers (Figure S32).

***In vivo* safety evaluation.** To evaluate the potential toxic effects of the nanocarriers, the mice were sacrificed on Day 1 and Day 14 after *i.v.* administration with different formulations and blood samples were collected for blood biochemistry and hematology analysis. Compared with the control group, all the liver function related markers (ALT, AST and ALP) increased significantly in mice at 24 h after injection of ALA-nMVs or ALA-hMVs (Fig. 7A–C). However, the liver function markers in ALA-hMVs treated mice decreased to normal levels after 14 days, while

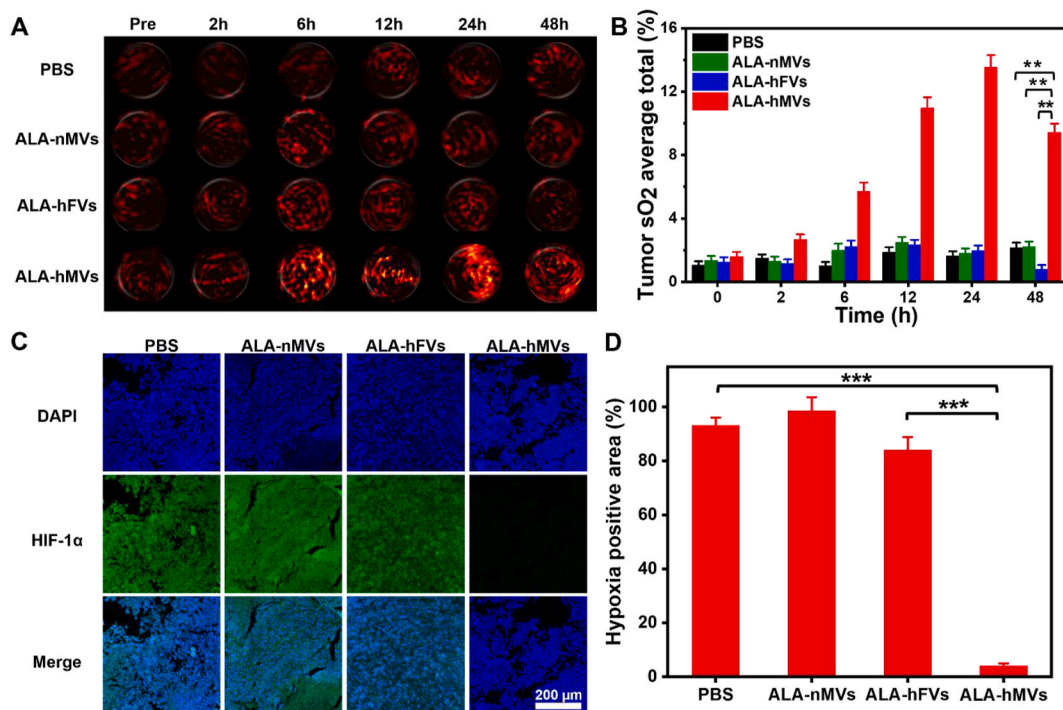


Fig. 5. *In vivo* hypoxia relief in B16 tumors by ALA-hMVs. (A) Representative PA images of B16 tumors on mice showing signals of oxygenated hemoglobin ($\lambda = 850$ nm) before/after *i.v.* injection of PBS, ALA-nMVs, ALA-hFVs and ALA-hMVs, respectively. (B) The corresponding quantification of the tumor vascular saturated O₂ levels (sO₂) calculated from (A). (C) Immunofluorescence staining of tumor sections showing expression of HIF-1 α after *i.v.* injection of PBS, ALA-nMVs, ALA-hFVs or ALA-hMVs, respectively. (D) Quantitative analysis of HIF-1 α positive areas for each group in (C) by using the ImageJ software (n = 5). (***p* < 0.01, ****p* < 0.001, ***p* < 0.05).

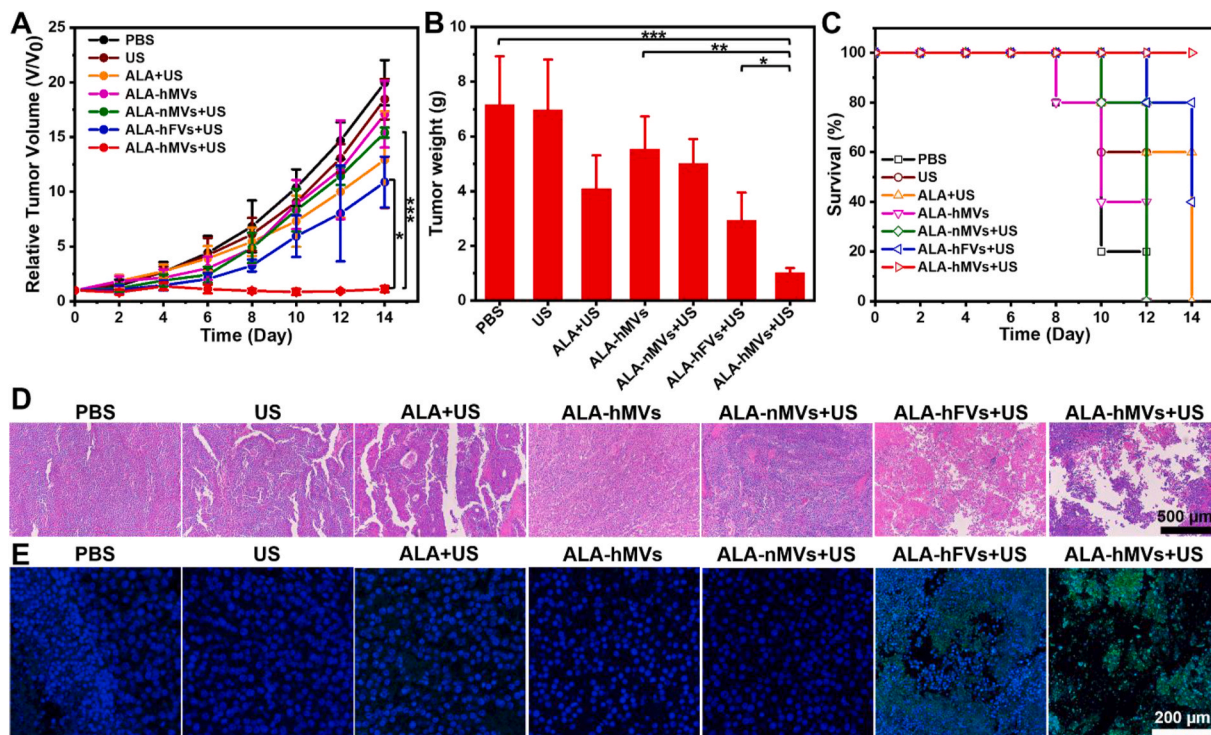


Fig. 6. Antitumor effect of ALA-hMVs-mediated SDT. (A) The tumor volume evolution curve, (B) the final tumor weight by the end of treatment and (C) survival curve of B16 tumor-bearing mice after different treatments. (D) H&E and (E) TUNEL staining of tumor sections collected from mice post various treatments. (***p* < 0.001, ***p* < 0.01, **p* < 0.05).

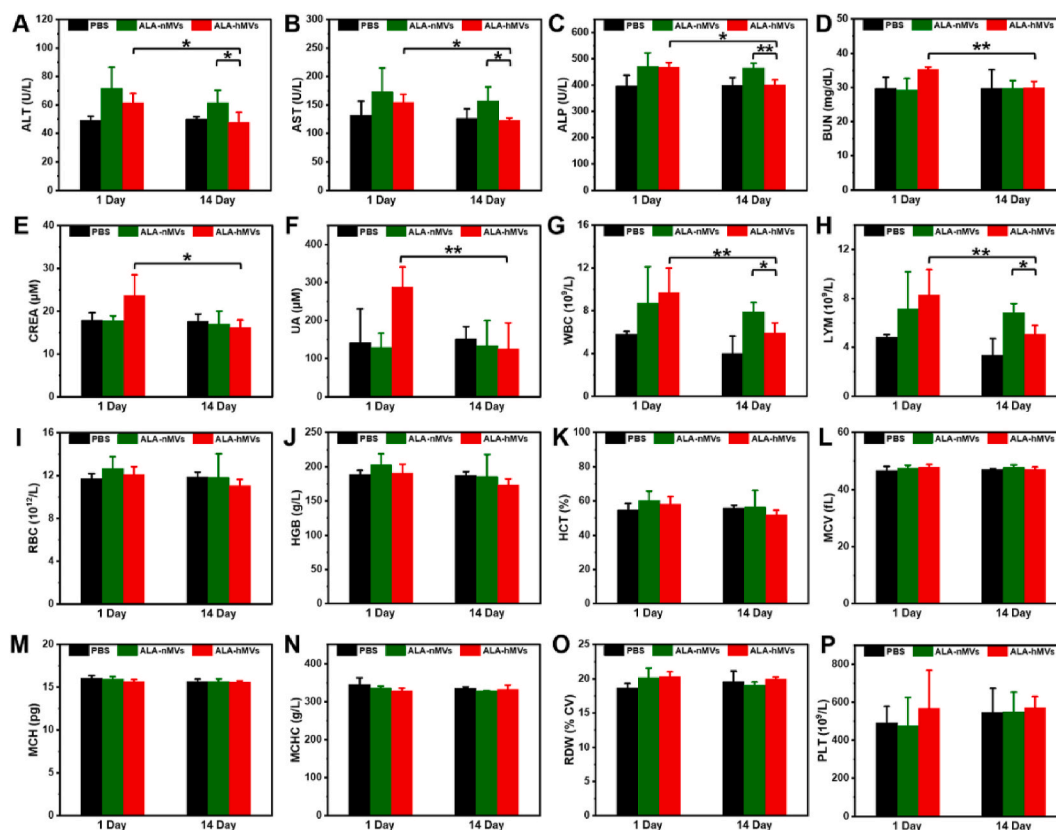


Fig. 7. Blood Biochemistry and Hematology Analysis. (A–C) Quantitative analysis of liver function biomarkers (ALT, AST and ALP) and (D–F) kidney function biomarkers (BUN, CREA and UA) in the blood of the mice intravenously administered with PBS, ALA-nMVs and ALA-hMVs, respectively. (G–P) The levels of (G) white blood cells, (H) lymphocytes, (I) red blood cells, (J) hemoglobin, (K) hematocrit, (L) mean corpuscular volume, (M) mean corpuscular hemoglobin, (N) mean corpuscular hemoglobin concentration, (O) red blood cell distribution width-standard deviation and (P) platelets in mice treated with PBS, ALA-nMVs and ALA-hMVs, respectively ($n = 5$). (***) $p < 0.001$, (**) $p < 0.01$, (*) $p < 0.05$. (For interpretation of the references to colour in this figure legend, the reader is referred to the Web version of this article.)

the markers remained in high levels in ALA-nMVs treated mice, indicating a long term liver damage in these mice. A temporary increase in kidney function markers (BUN, CREA and UA) was found in mice treated with ALA-hMVs, probably due to the renal clearance of dissociated MFNs (Fig. 7D–F). Compared with the control group, both ALA-nMVs and ALA-hMVs treated mice exhibited an increase in white blood cells (WBC) and lymphocytes (LYM) 24 h post-injection of the vesicles, suggesting an acute inflammatory response induced by the nanocarriers (Fig. 7G and H). The amount of WBC and LYM recovered to normal levels in ALA-hMVs treated mice after 14 days. However, ALA-nMVs treated mice still maintained a high level of WBC and LYM even after 14 days. Other hematological indicators, including red blood cell count (RBC), hemoglobin (HGB), hematocrit (HCT), mean corpuscular volume (MCV), mean corpuscular hemoglobin (MCH), mean corpuscular hemoglobin concentration (MCHC), red blood cell distribution width-standard deviation (RDW) and platelet count (PLT) showed no significant distinction to the control, confirming the desirable blood safety of the nanoassemblies (Fig. 7I–P). These results indicated that ALA-nMVs could induce long term liver damage and inflammation in mice, likely owing to the difficulty in clearance of these non-responsive vesicles. In contrast, no potential *in vivo* toxicity of ALA-hMVs was found under long-term treatment, suggesting the superior biosafety of the hypoxia-responsive nanocarriers.

3. Conclusion

In the current study, we have developed a hypoxia-responsive nanovesicle for tumor-specific generation of O_2 and delivery of

sonosensitizers to realize effective SDT of tumors. ALA-hMVs could rapidly dissociate into individual nanoparticles in the hypoxic TME and release ALA to induce ROS generation under US radiation. The dissociated MFNs acted as efficient catalysts to selectively generate O_2 in the tumor tissues to enhance O_2 -dependent SDT. Upon *in vivo* administration, ALA-hMVs exhibited much higher therapeutic efficacy in tumor elimination than non-responsive (ALA-nMVs) or non-catalytic but hypoxia-responsive nanocarriers (ALA-hFVs), suggesting that both hypoxia-responsiveness and catalytic oxygenation are essential for effective SDT of tumors. Furthermore, the released MFNs could be excreted from the body via renal clearance readily after the treatment, leading to minimized long term toxicity and superior biosafety of ALA-hMVs than the non-responsive vesicles.

In comparison with the conventional O_2 /sonosensitizer delivery platforms for SDT, ALA-hMVs could generate O_2 and release sonosensitizer ALA specifically in tumors by responding to the hypoxic TME, resulting in significantly enhanced SDT efficacy and reduced side effects under US radiation. The dissociated MFNs could be decomposed into ultra small nanoparticles *in vivo* so that they could be excreted from the body readily after the treatment via renal clearance, thus ensuring the great long term biosafety of the nanocarriers. This study not only provides a novel nano-assembly platform for effective SDT of highly hypoxic solid tumors, but also offers important new insights to the design and development of hypoxia-relieving materials for tumor microenvironment modulation and effective tumor treatment.

4. Methods

Materials: 2-Nitroimidazole, triethylamine (TEA), sodium hydroxide, hexamethylene bromohydrin, dimethyl sulfoxide (DMSO), methacryloyl chloride, styrene, poly(ethylene oxide) methyl ether (4-cyano-4-pentanoate dodecyl trithiocarbonate), 2,2'-Azobis(2-methylpropionitrile) (AIBN), n-butylamine, diethyl ether, tetrahydrofuran (THF), hexane, iron chloride (III) hexahydrate, manganese(II) chloride tetrahydrate, sodium oleate, 5-aminolevulinic acid hydrochloride (ALA), 2,2-Dimethoxy-2-phenylacetophenone (DMPA), 2,7-dichloro-fluorescein diacetate (DCFH-DA), hydrogen peroxide, thiazolyl blue tetrazolium bromide, fluorimetric hydrogen peroxide assay kit and annexin V-FITC/PI apoptosis detection kit were purchased from Sigma Aldrich and used without further purification. Dulbecco's modified Eagle's medium (DMEM), fetal bovine serum (FBS), PBS, trypsin-EDTA and penicillin/streptomycin (5000 U/mL) were purchased from Thermo Fisher Scientific.

Synthesis of the 6-(2-nitroimidazol-1-yl)hexyl methacrylate monomer. 2-Nitroimidazole (2.26 g, 20.0 mmol) and NaOH (0.800 g, 20.0 mmol) were mixed in 10 mL of DMSO and stirred at 50 °C for 1 h. Then hexamethylene bromohydrin (3.62 g, 20.0 mmol) was added into the mixture, stirred for 2 h, washed with water and extracted by ethyl acetate. The organic layer was collected and dried under vacuum, and the resultant compound (2.13 g, 10.0 mmol) was dissolved with methacryloyl chloride (4.16 g, 40.0 mmol) in 100 mL of dichloromethane, followed by dropwise addition of 5 mL of triethylamine under nitrogen atmosphere at 0 °C. The solution was stirred overnight and washed with water before collecting the organic layer for vacuum drying. The compound was further purified by flash column chromatography to obtain 6-(2-nitroimidazol-1-yl)hexyl methacrylate monomer with a yield of 44%. The ¹H NMR spectrum of the monomers is shown in Supporting Information. ¹H NMR (300 MHz, DMSO-*d*₆, 293 K) δ (ppm): 7.15 (d, *J* = 3 Hz, 1H), 7.08 (d, *J* = 3 Hz, 1H), 6.11–6.08 (m, 1H), 5.58–5.55 (m, 1H), 4.41 (t, *J* = 6 Hz, 2H), 4.14 (t, *J* = 6 Hz, 2H), 1.95 (s, 3H), 1.90–1.84 (m, 2H), 1.71–1.65 (m, 2H), 1.47–1.37 (m, 4H).

Synthesis of thiol-terminated and hypoxia-responsive BCPs. Thiol-terminated BCPs of SH-PNIHM₃₆-*b*-PEO₄₅ were synthesized as reported previously [38]. The molecular weight of the BCPs was 12.1 kg/mol as characterized by ¹H NMR by comparing the integrals of the resonance peaks of nitroimidazol of PNIHM block (7.0–7.2 ppm) and the methylene groups of PEO-CTA (3.65 ppm).

Synthesis of oleic acid-capped nanoparticles. Hydrophobic MFNs were prepared via thermal decomposition of iron oleate and manganese oleate complex by using oleic acid (OA) as the capping agent [24]. The resultant MFNs solution was washed with ethanol and re-dispersed in THF at a concentration of 5 mg/mL.

Synthesis of BCP-MFNs. Thiol-terminated BCPs were tethered onto OA-capped MFNs via an ultraviolet-induced thiol-ene reaction [26]. The resultant BCP-tethered MFNs were washed with THF for 3 times, collected by centrifugation (18000 rpm, 15min) and re-dispersed in THF at a concentration of 0.2 mg/mL. The hydrodynamic diameter of NPs in THF before and after BCPs attachment was measured using a PHOTOCOR-FC dynamic light scattering instrument (DLS). Thermogravimetric analysis (TGA) was performed to estimate the grafting density of BCPs on the surface of MFNs as reported previously [38].

Fabrication and characterization of hMVs, nMVs and hFVs. For the preparation of hMVs, 0.3 mL ultrapure water was added dropwise into 1 mL THF solution containing 0.4 mg BCP-MFNs by a syringe pump at rate of 2 mL/h. The solution was mixed under vortex for 6 h before dialysis against ultrapure water for removal of the organic solvent. The resultant hMVs were collected by centrifugation (2000 rpm, 15min) and imaged using a Hitachi SU-70 Schottky field emission gun Scanning Electron Microscope (FEG-SEM) and a JEOL FEG Transmission Electron Microscope (FEG-TEM). The hydrodynamic diameter of hMVs was evaluated by DLS. The stability of hMVs was evaluated by measuring their hydrodynamic diameters in PBS supplemented with 10% fetal

bovine serum for 30 days. Instead of ultrapure water, 0.3 mL ALA solution (5 mg/mL) was added dropwise into the THF solution of BCP-MFNs to obtain ALA-hMVs. The solution was purified by centrifugation for three times before further usage to remove unloaded ALA. nMVs and hFVs were prepared and characterized similarly except that the former was assembled from hypoxia-inert BCPs of PS₉₈-*b*-PEO₄₅ (12.2 kg/mol) and the latter used non-catalytic iron oxide nanoparticles as building blocks to construct ALA-loaded vesicles.

Hypoxia-responsive dissociation of hMVs. To investigate the hypoxia-responsiveness of the monomers, 6-(2-nitroimidazol-1-yl)hexyl methacrylate was incubated with 100 μM NADH and 5 μg/mL nitroreductase under nitrogen to simulate the hypoxic TME. A 50 μL aliquots of the sample was analyzed by HPLC after various incubation time with the mobile phase (20% methanol, 80% water) pumped at a flow rate of 1 mL/min. To verify the hypoxia-responsiveness of the assemblies, hMVs were incubated with 100 μM NADH and 5 μg/mL nitroreductase under nitrogen. The morphology and hydrodynamic diameter of hMVs were evaluated by TEM and DLS at scheduled time intervals to reveal the hypoxia-responsiveness of the nano-assemblies. To monitor the release behaviors of ALA-hMVs under different conditions, 1 mL solution of ALA-MVs was transferred into a dialysis tube (MWCO: 6000–8000) and incubated in 50 mL PBS at 37 °C under nitrogen with and without nitroreductase and NADH, respectively. One milliliter of PBS was taken at scheduled time points to evaluate the released amounts of ALA by using a fluorescamine-based fluorescence assay [39]. The 1 mL solution was returned to the reservoir after each measurement to maintain a constant volume of the buffer solution. The release behaviors of ALA-nMVs and ALA-hFVs was also measured as controls.

O₂ generation catalyzed by dissociated hMVs in the presence of H₂O₂. To evaluate the catalytic capacity of the vesicles, hMVs were incubated with 100 μM NADH and 5 μg/mL nitroreductase under nitrogen for 2 h, followed by the addition of H₂O₂ (100 μM). After various time intervals, the consumption of H₂O₂ and generation of O₂ were measured by a fluorimetric hydrogen peroxide assay kit and a dissolved oxygen meter, respectively. For comparison, hMVs were treated with PBS before addition of H₂O₂ and measurement of H₂O₂ and O₂ concentrations. The generation of O₂ in the presence of nMVs or hFVs under normoxia or hypoxia was also evaluated as controls. The continuous catalytic effect of dissociated hMVs was verified by incubating hMVs with 100 μM NADH and 5 μg/mL nitroreductase under nitrogen for 2 h, followed by repetitive addition of H₂O₂ to the solution for 4 rounds. The concentration of H₂O₂ in the solution was measured 3 h after each addition of H₂O₂ by using a fluorimetric hydrogen peroxide assay kit.

Hypoxia-induced dissociation of hMVs in vitro. For direct observation of hMVs after cellular internalization, the mouse melanoma cell line (B16) were grown on Thermanox® Plastic Coverslips and incubated with hMVs for 48 h under normoxic and hypoxic conditions respectively. The culture media were replaced with the fixation solution and washed with 0.1 M sodium cacodylate buffer. The samples were dehydrated and polymerized at 60 °C for 24 h before collecting the ultrathin sections of the cells on a Leica EM UC6 Ultramicrotome (Leica, Buffalo Grove, IL) for TEM observations.

Hypoxia relief by dissociated hMVs in vitro. To evaluate the relief of hypoxia by hMVs *in vitro*, B16 cells were incubated under normoxic or hypoxic conditions for 48 h, followed by the addition of hMVs into the culture media. After incubation for another 24 h in normoxia or hypoxia respectively, the culture media were replaced, followed by the addition of anti-HIF-1α antibody (dilution 1:200) and Cy5-conjugated goat anti-mouse secondary antibody (dilution 1:200). Then the cells were washed with PBS, stained with Hoechst and imaged under a confocal microscope (Zeiss LSM 710). For comparison, B16 cells were also incubated with PBS, nMVs or hFVs in normoxia and hypoxia, respectively. The expression of HIF-1α in the cells were evaluated and compared with that in hMVs-treated cells.

Cellular uptake and conversion of ALA into PpIX in vitro. B16 cells were first incubated under normoxic or hypoxic conditions for 48 h.

Thereafter, the culture media were replaced with fresh media containing PBS, ALA, ALA-nMVs, ALA-hFVs or ALA-hMVs respectively. The cells were further incubated for 2 h, 6 h, 12 h and 24 h, respectively. Then the cells were washed with PBS and stained with Hoechst under dark for 15 min. After washing, the cells were observed by a confocal microscope to monitor the red fluorescence from PpIX transformed by the released ALA. Subsequently, DMSO was used to extract cellular PpIX, whose fluorescent intensity at 635 nm was measured using a spectrofluorometer (FluoroMax-4, HORIBA, Japan).

Detection of intracellular ROS. To evaluate the intracellular production of ROS, B16 cells were first incubated under normoxic or hypoxic conditions for 48 h. The culture media were replaced with fresh media containing PBS, ALA, hMVs, ALA-nMVs, ALA-hFVs or ALA-hMVs respectively. The cells were further incubated for 12 h before irradiated by US (1.0 MHz, 1.5 W cm⁻², 30 s, 50% duty cycle). After washed with PBS and stained with DCFH-DA for 20 min, the ROS fluorescence in B16 cells were observed by a confocal microscope. Then the cells were treated with DMSO and the fluorescent intensity at 535 nm was measured by a spectrofluorometer. The cells incubated with PBS, ALA or ALA-loaded vesicles in the absence of US were used as controls.

Cytotoxicity Assay. Cytotoxicity of ALA-loaded vesicles on B16 cells were evaluated using the MTT assay [34]. Briefly, B16 cells were cultured in normoxia or hypoxia for 48 h before replacement of the culture media with fresh media containing gradient concentrations of ALA, hMVs, ALA-nMVs, ALA-hFVs or ALA-hMVs. The cells were further incubated for 12 h, washed with PBS, irradiated by US and cultured for another 24 h before the MTT assay. The absorbance of each well at 570 and 650 nm was measured by using a microplate reader (SpectraMax M5) to estimate the cell viabilities as a function of ALA concentrations. Viability of cells in the absence of US was also measured as controls.

Apoptotic/Necrotic Assay. An Annexin V-FITC/PI apoptosis detection kit was applied to assess the cell apoptotic/necrotic rate. Briefly, B16 cells were first incubated under normoxic or hypoxic conditions for 48 h. Then the culture medium was replaced with fresh media containing PBS, ALA, hMVs, ALA-nMVs, ALA-hFVs or ALA-hMVs and further cultured for 12 h. The cells was washed with PBS and irradiated by US before cultured for another 24 h. Then the cells were stained with annexin V-FITC and PI in the dark, followed by washing and collection for flow cytometry analysis (CytoFLEX, Beckman, USA).

In Vivo biodistribution of ALA-hMVs. All animal experiments were performed under an ICMS Ethics Committee (University of Macau) approved protocol. Tumor-bearing mice were obtained by subcutaneously injecting $\sim 2 \times 10^6$ B16 cells into the right hind leg of female C57BL/6 mice. Cy7-amine was conjugated to COOH-PEO-*b*-PNIHM-SH for the synthesis of Cy7-labeled BCPs. Cy7-labeled, ALA-loaded hMVs (Cy7-ALA-hMVs) were prepared by using Cy7-labeled BCPs for the assembly of vesicles. When the tumor volume exceeded 100 mm³, Cy7-ALA-hMVs (50 mg/kg ALA) were intravenously injected into the tumor-bearing mice (n = 5) and whole-animal imaging was recorded at scheduled time points by using an *in vivo* imaging system (Lumina XR, Caliper, USA) to monitor the fluorescence from Cy7. The mice were sacrificed at 48 h post-injection of Cy7-ALA-hMVs to collect the tumors and major organs. The average fluorescence intensities from Cy7 in tumors and major organs was evaluated to reveal the *in vivo* biodistribution of the Cy7-ALA-hMVs. To further evaluate detailed *in vivo* distribution of ALA-hMVs, B16 tumor bearing mice were intravenously injected with ALA-hMVs and the content of Mn in blood and major organs were measured by ICP-MS. To investigate the renal clearance of dissociated MFNs, mice urine was collected at scheduled time and the content of Mn in urine was measured by ICP-MS. MFNs in mice urine at 24 h post-injection of ALA-hMVs were desalted and purified through centrifugal ultrafiltration for TEM imaging.

In vivo hypoxia relief by ALA-hMVs. PA imaging was used to reveal the tumor vascular saturated O₂ levels (sO₂). Briefly, tumor-bearing mice were intravenously administered with ALA-hMVs (50 mg/kg ALA) and PA imaging of the tumor region was recorded at 2, 6, 12, 24,

48 h post injection via a multispectral PA imaging system. In another test, tumor-bearing mice were intravenously injected with ALA-hMVs (50 mg/kg ALA) and sacrificed 48 h post-injection for tumor collection (n = 5). Frozen sections of the tumors were prepared for immunofluorescence staining of HIF-1 α and the corresponding tumor sections were observed by a confocal microscope. Quantification of tumor hypoxia by analysis of fluorescence signals from the immunofluorescence staining images was performed with ImageJ software.

In vivo sonodynamic therapy of ALA-hMVs. B16 tumor-bearing mice were separated in a random manner into seven groups (n = 5): i) PBS; ii) US; iii) ALA + US; iv) ALA-hMVs; v) ALA-nMVs + US; vi) ALA-hFVs + US and vii) ALA-hMVs + US. At 24 h after *i.v.* injection on Day 0 and Day3, the tumors were applied with US radiation. During the treatment period, the tumor volume was closely monitored every two days. The body weight and survival rate of the mice was also assessed during the treatment period. At the end of the treatment, tumors were collected for weighing, H&E and TUNEL staining. Major organs of mice were also collected for H&E staining to evaluate the biosafety of the treatments.

In vivo safety evaluation. B16 tumor-bearing mice were intravenously injected with PBS, ALA-nMVs and ALA-hMVs, respectively (n = 5). At 24 h and 14 days post injection, the blood of each mouse was collected for pathological and biochemistry studies. The blood panel parameters of the mice were also evaluated using standard hematology test.

Statistical analysis. All results are expressed as means \pm SD. as indicated. A one-way analysis of variance (ANOVA) test was performed to compare differences between groups. Statistical significance was considered at *P < 0.05, **P < 0.01, ***P < 0.001.

Declaration of competing interest

The authors declare that they have no known competing financial interests or personal relationships that could have appeared to influence the work reported in this paper.

Acknowledgements

This study was financially supported by the Science and Technology Development Fund, Macau SAR (File no.: 0121/2018/A3 and SKL-QRCM(UM)-2020-2022), University of Macau (File no.: MYRG2017-00010-ICMS and MYRG2019-00059-ICMS), the National University of Singapore start-up fund (NUHSRO/2020/133/Startup/08) and NUS School of Medicine Nanomedicine Translational Research Programme (NUHSRO/2021/034/TRP/09/Nanomedicine). K.Y. is supported by the UM Macao Postdoctoral Fellowship.

Appendix A. Supplementary data

Supplementary data to this article can be found online at <https://doi.org/10.1016/j.biomaterials.2021.120822>.

Author statement

K. Y., L.Y. and Z. Y. contributed equally to this work. K. Y., X. C. and R. W. conceived this project. K. Y. performed most of the experiments, analyzed the results, and drafted the manuscript. L. Y. and Z. Y. performed *in vivo* experiments and analyzed the data. G. Y., L. R., R. T. and Z. Y. synthesised and characterised the hypoxia-responsive block-copolymers. J. W. designed schemes and assisted in preparing figures in the manuscript. C. S., X. Z., M. X. and J. M. assisted with *in vivo* experiments.

References

- [1] I. Rosenthal, J.Z. Sostaric, P. Riesz, Sonodynamic therapy—a review of the synergistic effects of drugs and ultrasound, *Ultrason. Sonochem.* 11 (6) (2004) 349–363.
- [2] X. Qian, Y. Zheng, Y. Chen, Micro/nanoparticle-augmented sonodynamic therapy (SDT): breaking the depth shallow of photoactivation, *Adv. Mater.* 28 (37) (2016) 8097–8129.
- [3] M. Trendowski, The promise of sonodynamic therapy, *Cancer Metastasis Rev* 33 (1) (2014) 143–160.
- [4] H. Chen, X. Zhou, Y. Gao, B. Zheng, F. Tang, J. Huang, Recent progress in development of new sonosensitizers for sonodynamic cancer therapy, *Drug Discov. Today* 19 (4) (2014) 502–509.
- [5] X. Lin, S. Liu, X. Zhang, R. Zhu, S. Chen, X. Chen, et al., An ultrasound activated vesicle of janus Au-MnO nanoparticles for promoted tumor penetration and sonochemodynamic therapy of orthotopic liver cancer, *Angew. Chem. Int. Ed.* 59 (4) (2020) 1682–1688.
- [6] P. Huang, X. Qian, Y. Chen, L. Yu, H. Lin, L. Wang, et al., Metalloporphyrin-encapsulated biodegradable nanosystems for highly efficient magnetic resonance imaging-guided sonodynamic cancer therapy, *J. Am. Chem. Soc.* 139 (3) (2017) 1275–1284.
- [7] W. Yue, L. Chen, L. Yu, B. Zhou, H. Yin, W. Ren, et al., Checkpoint blockade and nanosensitizer-augmented noninvasive sonodynamic therapy combination reduces tumour growth and metastases in mice, *Nat. Commun.* 10 (1) (2019) 2025.
- [8] Y. Wang, Y. Liu, H. Wu, J. Zhang, Q. Tian, S. Yang, Functionalized holmium-doped hollow silica nanospheres for combined sonodynamic and hypoxia-activated therapy, *Adv. Funct. Mater.* 29 (3) (2019) 1805764.
- [9] Y. Sheng, E. Beguin, H. Nesbitt, S. Kamila, J. Owen, L.C. Barnsley, et al., Magnetically responsive microbubbles as delivery vehicles for targeted sonodynamic and antimetabolite therapy of pancreatic cancer, *J. Controlled Release* 262 (2017) 192–200.
- [10] P. Zhu, Y. Chen, J. Shi, Nanoenzyme-augmented cancer sonodynamic therapy by catalytic tumor oxygenation, *ACS Nano* 12 (4) (2018) 3780–3795.
- [11] D. Sun, X. Pang, Y. Cheng, J. Ming, S. Xiang, C. Zhang, et al., Ultrasound-switchable nanozyme augments sonodynamic therapy against multidrug-resistant bacterial infection, *ACS Nano* 14 (2) (2020) 2063–2076.
- [12] G. Li, S. Wang, D. Deng, Z. Xiao, Z. Dong, Z. Wang, et al., Fluorinated chitosan to enhance transmucosal delivery of sonosensitizer-conjugated catalase for sonodynamic bladder cancer treatment post-intravesical instillation, *ACS Nano* 14 (2) (2020) 1586–1599.
- [13] X. Pan, W. Wang, Z. Huang, S. Liu, J. Guo, F. Zhang, et al., MOF-derived double-layer hollow nanoparticles with oxygen generation ability for multimodal imaging-guided sonodynamic therapy, *Angew. Chem. Int. Ed.* 59 (32) (2020) 13557–13561.
- [14] J. Chen, H. Luo, Y. Liu, W. Zhang, H. Li, T. Luo, et al., Oxygen-self-produced nanoplatfor for relieving hypoxia and breaking resistance to sonodynamic treatment of pancreatic cancer, *ACS Nano* 11 (12) (2017) 12849–12862.
- [15] J. Fu, T. Li, Y. Zhu, Y. Hao, Ultrasound-activated oxygen and ROS generation nanosystem systematically modulates tumor microenvironment and sensitizes sonodynamic therapy for hypoxic solid tumors, *Adv. Funct. Mater.* 29 (51) (2019) 1906195.
- [16] C.G. Hadjipanayis, W. Stummer, 5-ALA and FDA approval for glioma surgery, *J. Neuro Oncol.* 141 (3) (2019) 479–486.
- [17] C. Qian, J. Yu, Y. Chen, Q. Hu, X. Xiao, W. Sun, et al., Light-activated hypoxia-responsive nanocarriers for enhanced anticancer therapy, *Adv. Mater.* 28 (17) (2016) 3313–3320.
- [18] J. Yu, Y. Zhang, Y. Ye, R. DiSanto, W. Sun, D. Ranson, et al., Microneedle-array patches loaded with hypoxia-sensitive vesicles provide fast glucose-responsive insulin delivery, *Proc. Natl. Acad. Sci.* 112 (27) (2015) 8260.
- [19] T. Thambi, V.G. Deepagan, H.Y. Yoon, H.S. Han, S.-H. Kim, S. Son, et al., Hypoxia-responsive polymeric nanoparticles for tumor-targeted drug delivery, *Biomaterials* 35 (5) (2014) 1735–1743.
- [20] L. Wang, Y. Hu, Y. Hao, L. Li, C. Zheng, H. Zhao, et al., Tumor-targeting core-shell structured nanoparticles for drug procedural controlled release and cancer sonodynamic combined therapy, *J. Controlled Release* 286 (2018) 74–84.
- [21] C. Suzuki, A.B. Tsuji, K. Kato, T. Kikuchi, H. Sudo, M. Okada, et al., Preclinical characterization of 5-amino-4-oxo-[6-¹¹C]hexanoic acid as an imaging probe to estimate protoporphyrin IX accumulation induced by exogenous aminolevulinic acid, *J. Nucl. Med.* 55 (10) (2014) 1671–1677.
- [22] J. Kim, H.R. Cho, H. Jeon, D. Kim, C. Song, N. Lee, et al., Continuous O₂-evolving MnFe₂O₄ nanoparticle-anchored mesoporous silica nanoparticles for efficient photodynamic therapy in hypoxic cancer, *J. Am. Chem. Soc.* 139 (32) (2017) 10992–10995.
- [23] S.-Y. Yin, G. Song, Y. Yang, Y. Zhao, P. Wang, L.-M. Zhu, et al., Persistent regulation of tumor microenvironment by circulating catalysis of MnFe₂O₄@Metal-organic frameworks for enhanced photodynamic therapy, *Adv. Funct. Mater.* 29 (25) (2019) 1901417.
- [24] J. Park, K. An, Y. Hwang, J.-G. Park, H.-J. Noh, J.-Y. Kim, et al., Ultra-large-scale syntheses of monodisperse nanocrystals, *Nat. Mater.* 3 (12) (2004) 891–895.
- [25] J. He, X. Huang, Y.-C. Li, Y. Liu, T. Babu, M.A. Aronova, et al., Self-assembly of amphiphilic plasmonic micelle-like nanoparticles in selective solvents, *J. Am. Chem. Soc.* 135 (21) (2013) 7974–7984.
- [26] B. Liu, X. Deng, Z. Xie, Z. Cheng, P. Yang, J. Lin, Thiol-ene click reaction as a facile and general approach for surface functionalization of colloidal nanocrystals, *Adv. Mater.* 29 (36) (2017) 1604878.
- [27] X. Ye, C. Zhu, P. Ercius, S.N. Raja, B. He, M.R. Jones, et al., Structural diversity in binary superlattices self-assembled from polymer-grafted nanocrystals, *Nat. Commun.* 6 (1) (2015) 10052.
- [28] J. He, Y. Liu, T. Babu, Z. Wei, Z. Nie, Self-assembly of inorganic nanoparticle vesicles and tubules driven by tethered linear block copolymers, *J. Am. Chem. Soc.* 134 (28) (2012) 11342–11345.
- [29] J. He, Z. Wei, L. Wang, Z. Tomova, T. Babu, C. Wang, et al., Hydrodynamically driven self-assembly of giant vesicles of metal nanoparticles for remote-controlled release, *Angew. Chem. Int. Ed.* 52 (9) (2013) 2463–2468.
- [30] R.K. Jain, T. Stylianopoulos, Delivering nanomedicine to solid tumors, *Nat. Rev. Clin. Oncol.* 7 (11) (2010) 653–664.
- [31] A. Albanese, P.S. Tang, W.C.W. Chan, The effect of nanoparticle size, shape, and surface chemistry on Biological systems, *Annu. Rev. Biomed. Eng.* 14 (1) (2012) 1–16.
- [32] G.L. Wang, B.H. Jiang, E.A. Rue, G.L. Semenza, Hypoxia-inducible factor 1 is a basic-helix-loop-helix-PAS heterodimer regulated by cellular O₂ tension, *Proc. Natl. Acad. Sci. U. S. A.* 92 (12) (1995) 5510.
- [33] G.L. Semenza, Targeting HIF-1 for cancer therapy, *Nat. Rev. Cancer* 3 (10) (2003) 721–732.
- [34] T. Mosmann, Rapid colorimetric assay for cellular growth and survival: application to proliferation and cytotoxicity assays, *J. Immunol. Methods* 65 (1) (1983) 55–63.
- [35] J. Liu, M. Yu, C. Zhou, J. Zheng, Renal clearable inorganic nanoparticles: a new frontier of bionanotechnology, *Mater. Today (Kidlington)* 16 (12) (2013) 477–486.
- [36] E.B. Ehlerding, F. Chen, W. Cai, Biodegradable and renal clearable inorganic nanoparticles, *Adv. Sci.* 3 (2) (2016) 1500223.
- [37] S. Tang, M. Chen, N. Zheng, Sub-10-nm Pd nanosheets with renal clearance for efficient near-infrared photothermal cancer therapy, *Small* 10 (15) (2014) 3139–3144.
- [38] K. Yang, G. Yu, R. Tian, Z. Zhou, H. Deng, L. Li, et al., Oxygen-evolving manganese ferrite nanovesicles for hypoxia-responsive drug delivery and enhanced cancer chemioimmunotherapy, *Adv. Funct. Mater.* 31 (2021) 2008078.
- [39] A.K. Jain, C.H. Lee, H.S. Gill, 5-Aminolevulinic acid coated microneedles for photodynamic therapy of skin tumors, *J. Control. Release* 239 (2016) 72–81.